# Supporting Information

## Engineering Active Ni Sites in Ternary Layered Double Hydroxide Nanosheets for a High Selectivity Photoreduction of $CO_2$ to $CH_4$ under Irradiation above 500 nm

Xiaojie Hao,[a] Ling Tan,[a] Yanqi Xu,[a] Zelin Wang,[a] Xian Wang,[a] Sha Bai,[a] Chenjun Ning,[a] Jingwen Zhao,[b] Yufei Zhao,[a]* Yu-Fei Song[a]*

[a]*State Key Laboratory of Chemical Resource Engineering and Beijing Advanced Innovation Center for Soft Matter Science and Engineering, Beijing University of Chemical Technology, Beijing, 100029, People's Republic of China.*

[b]*Qingdao Institute of Bioenergy and Bioprocess Technology, Chinese Academy of Sciences, Qingdao, 266101, P. R. China.*

## Experimental

**Materials:** $Ni(NO_3)_2 \cdot 6H_2O$, $Co(NO_3)_2 \cdot 6H_2O$, $Fe(NO_3)_3 \cdot 9H_2O$, $FeSO_4 \cdot 7H_2O$, NaOH, $[Ru(bpy)_3]Cl_2 \cdot 6H_2O$ (bpy = 2'2-bipyridine), Triethanolamine (TEOA) and acetonitrile (MeCN) were purchased from Energy Chemical and were used directly without any further purification. Deionized water was used in all the experimental processes.

**Synthesis of CoFe-LDH nanosheets:** The CoFe-LDH nanosheets were typically prepared via a co-precipitation process. To prepare solution A, 32 mmol $Co(NO_3)_2 \cdot 6H_2O$ and 10.7 mmol $FeSO_4 \cdot 7H_2O$ were dissolved in 40 mL deionized water to form a homogeneous solution (Co : Fe = 3 : 1). Solution B was prepared by dissolving 68.3 mmol NaOH and 21.3 mmol $NaNO_3$ in 40 mL deionized water (the deionized water was boiled to remove dissolved carbon dioxide and kept at 60℃ for use). Solutions A and B were simultaneously added dropwise to a beaker containing 80 mL deionized water until the pH of the final solution was adjusted to 8.5. After stirring for another 24 h at 40℃, a solid precipitate was formed and collected by centrifugation and then washed three times with water. The collected samples were dried in an oven at 60℃ overnight.

**Synthesis of NiCoFe-LDH nanosheets:** The NiCoFe-LDH nanosheets were typically prepared via a co-precipitation process. To prepare solution A, 16 mmol $Co(NO_3)_2 \cdot 6H_2O$, 16 mmol $Ni(NO_3)_2 \cdot 6H_2O$ and 10.7 mmol $Fe(NO_3)_3 \cdot 9H_2O$ were dissolved in 40 mL deionized water to form a homogeneous solution (Co : Ni : Fe = 1.5 : 1.5 : 1). Solution B was prepared by dissolving 68.3 mmol NaOH and 21.3 mmol $NaNO_3$ in 40 mL deionized water (the deionized water was boiled to remove dissolved carbon dioxide and kept at 60℃ for use). Solutions A and B were simultaneously added dropwise to a beaker containing 80 mL deionized water until the pH of the final solution was adjusted to 8.5. After stirring for another 24 h at 40℃, a solid precipitate was formed and collected by centrifugation and then washed three times with water. The collected samples were dried in an oven at 60℃ overnight.

**Synthesis of NiFe-LDH nanosheets:** The NiFe-LDH nanosheets were typically prepared via a co-precipitation process. To prepare solution A, 32 mmol $Ni(NO_3)_2 \cdot 6H_2O$ and 10.7 mmol $Fe(NO_3)_3 \cdot 9H_2O$ were dissolved in 40 mL deionized water to form a homogeneous solution (Ni: Fe = 3: 1). Solution B was prepared by dissolving 68.3 mmol NaOH and 21.3 mmol $NaNO_3$ in 40 mL deionized water (the deionized water was boiled to remove dissolved carbon dioxide and kept at 60℃ for use). Solutions A and B were simultaneously added dropwise to a beaker containing 80 mL deionized water until the pH of the final solution was adjusted to 8.5. After stirring for another 24 h at 40℃, a solid precipitate was formed and collected by centrifugation and then washed three times with water. The collected samples were dried in an oven at 60℃ overnight.

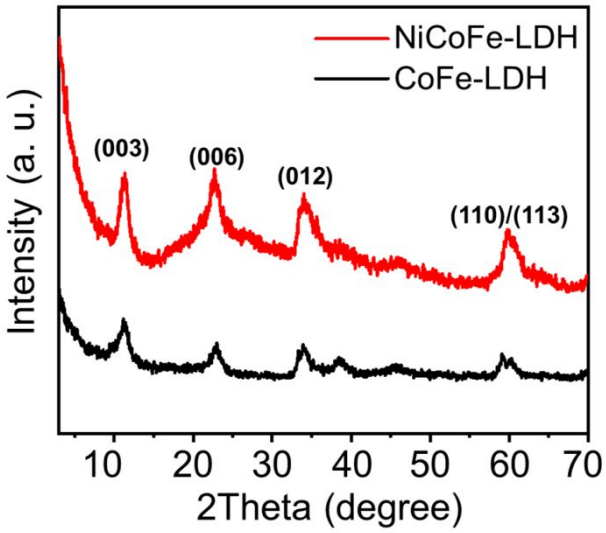


**Figure S1.** XRD patterns of CoFe-LDH and NiCoFe-LDH.

XRD patterns of CoFe-LDH and NiCoFe-LDH were displayed in Figure S1. XRD data of the NiCoFe-LDH (red line) and CoFe-LDH (black line) showed a series of (003), (006), (012), (110), and (113) diffractions of LDHs phase of the CoFe-LDH and NiCoFe-LDH at $2\theta = 11.5°$, 22.9°, 34.5°, 59.8°, and 61.2°, respectively, indicating that the successful synthesis of LDHs.

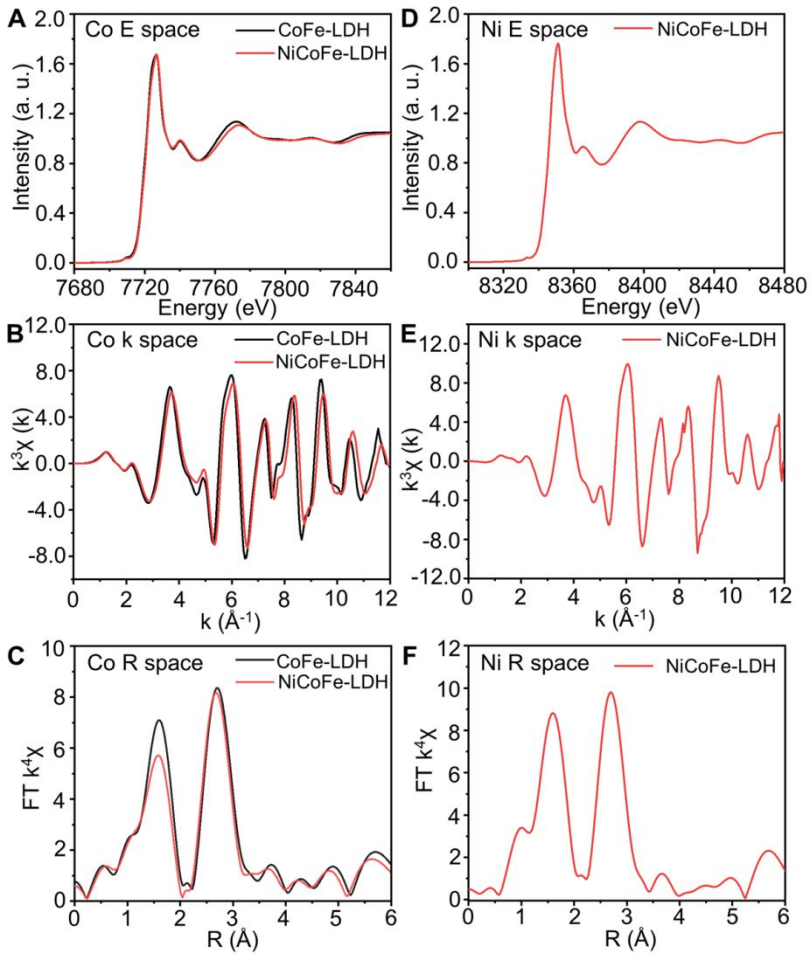


**Figure S2.** (A) Co K-edge XANES spectra, (B) Co K-edge EXAFS oscillation functions $k^3\chi$ (k), (C) magnitude of $k^3$-weighted FT of the Co K-edge extended EXAFS spectra and corresponding curve-fitting results (dotted lines), (D) Ni K-edge XANES spectra, (E) Ni K-edge EXAFS oscillation functions $k^3\chi$ (k), and (F) magnitude of $k^3$-weighted FT of the Ni K-edge EXAFS spectra and corresponding curve-fitting results (dotted lines) for NiCoFe-LDH and CoFe-LDH, respectively.

The doping mode of Ni is substitutional as proved by EXAFS and XRD. As shown in Figure S2F, the local coordination structure of Ni species is similar to Co species with a same peak position. These results indicated that Ni species should replace the site of Co. Thus, the doping mode of Ni is substitutional in LDH structure.

**Table S1.** Summary of Elemental Analysis Data for CoFe-LDH and NiCoFe-LDH, from ICP results

| Sample | Co (%) | Fe (%) | Ni (%) |
|---|---|---|---|
| **NiCoFe-LDH** | 19.7 | 12.5 | 19.6 |
| **CoFe-LDH** | 39.4 | 12.4 | 0 |

The doping amount of Ni can be determined through inductively coupled plasma atomic emission spectroscopy (ICP-AES) analysis. As shown in Table S1, the ratio of Co : Ni : Fe in NiCoFe-LDH was about 1.4 : 1.4 : 1, which is almost consistent with the feed ratio (1.5 : 1.5 : 1).

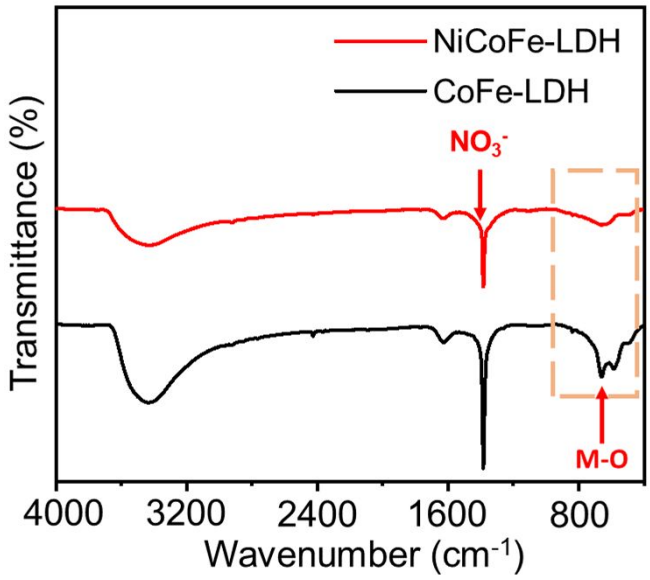


**Figure S3.** FT-IR spectra of CoFe-LDH and NiCoFe-LDH.

In the FT-IR spectrum (Figure S2), the broadband at 3430 $cm^{-1}$ was belonged to the stretching vibration and bending vibration of the O-H bond. The small pinnacle at 1633 $cm^{-1}$ was designated to interlayer water. The strong bond at 1380 $cm^{-1}$ signified the vibrations of $NO_3^-$. We can see the M-O bond vibration peak of at 580 $cm^{-1}$.

All the observation of XRD and FT-IR measurements revealed the successful synthesis of CoFe-LDH and NiCoFe-LDH structure with intercalated $NO_3^-$ anion.

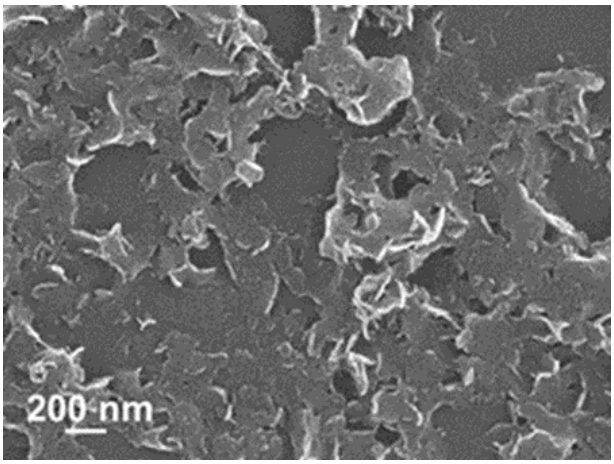


**Figure S4.** SEM image of NiCoFe-LDH

SEM image of NiCoFe-LDH (Figure S3) confirmed the formation of ultrathin sheet-like morphology.

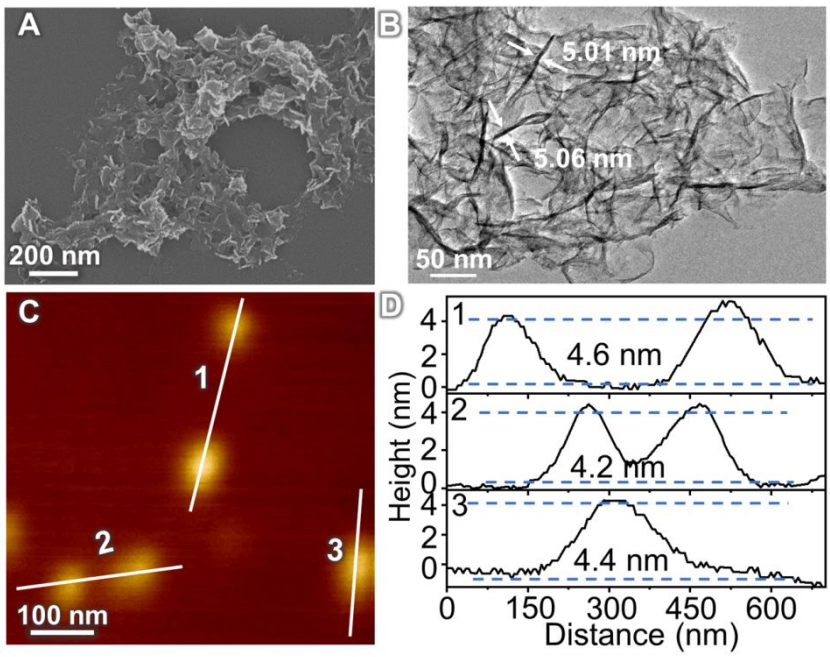


**Figure S5.** The (A) SEM images; (B) HRTEM image; (C) AFM image and the corresponding (D) height profiles of CoFe-LDH.

SEM and TEM images revealed a typical nanoplate structure with an average size of ≈ 80 nm for the CoFe-LDH, as shown in Figure S4A, B. The thickness of the CoFe-LDH nanosheets was determined to be only ≈ 5 nm. Atomic force microscopy (AFM) image in Figure S4C, D also revealed their average thickness of approximately 4.5 nm, corresponding to 5-6 monolayers in the nanostructure.

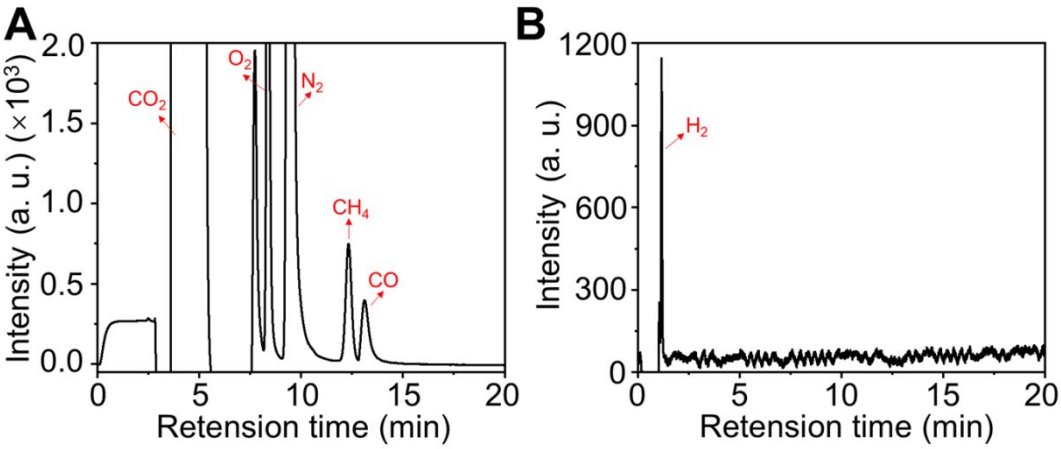


**Figure S6.** (A) TCD1 Chromatogram of carbon-containing products ($CH_4$, CO), (B) TCD2 Chromatogram of carbon-containing products ($H_2$) from photocatalytic $CO_2$ reduction on NiCoFe-LDH under visible light ($\lambda$ > 400 nm) for 1 h.

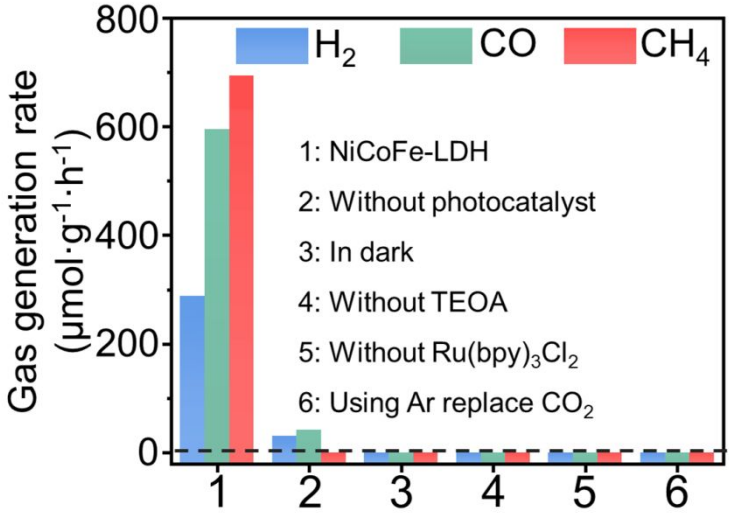


**Figure S7**. $CO_2$ reduction performance under various reaction conditions.

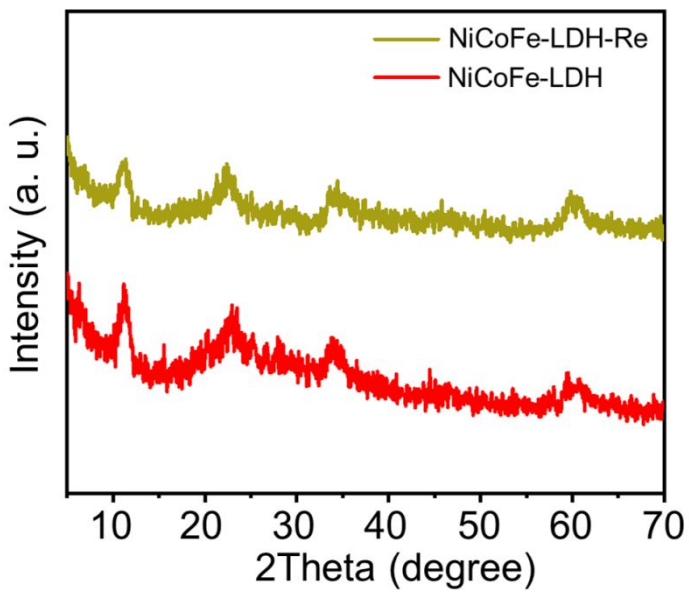


**Figure S8.** XRD patterns of the fresh NiCoFe-LDH sample and after the photocatalytic reaction (denoted as NiCoFe-LDH-Re).

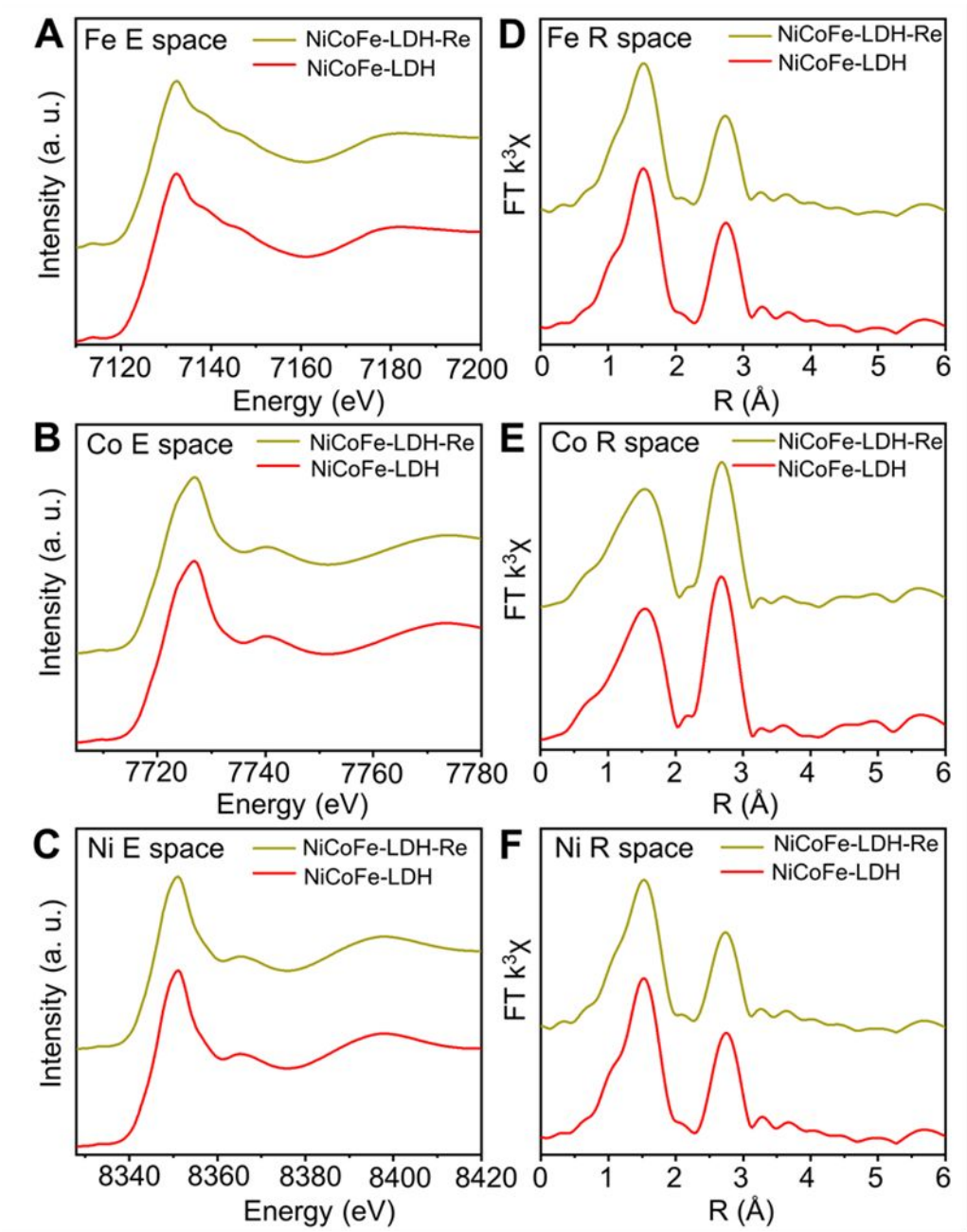


**Figure S9.** (A, B, C) Normalized Co, Fe, and Ni K-edge XANES spectra of the NiCoFe-LDH and NiCoFe-LDH-Re, respectively. (D, E, F) $k^3$-weighted Fourier-transform Co, Fe, and Ni K-edge EXAFS spectra, respectively.

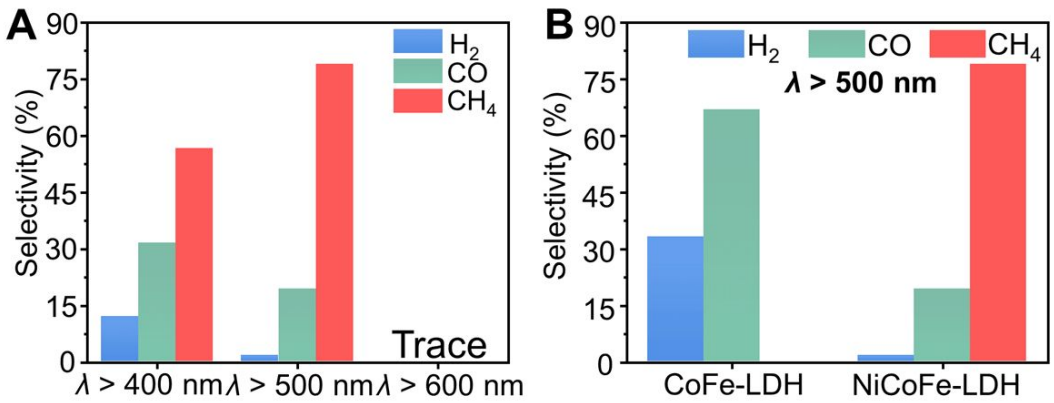


**Figure S10.** The (A) $CO_2$ conversion rate and (B) Selectivity of $CH_4$, CO and $H_2$ on NiCoFe-LDH under irradiation with different wavelength light.

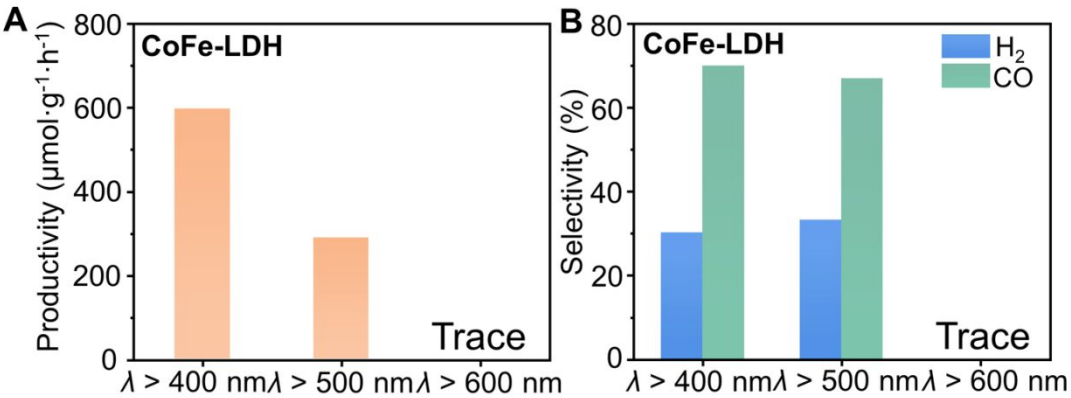


**Figure S11.** The (A) $CO_2$ conversion rate and (B) Selectivity of $CH_4$, CO, and $H_2$ on CoFe-LDH under irradiation with different wavelength light.

**Table S2.** Comparison of photocatalytic $CO_2$ reduction performance for various photocatalysts in this work and in previous literature

| | Catalyst | Photosensitizer | Sacrificial agent | Solvent | Light source | Selectivity | Reference |
|---|---|---|---|---|---|---|---|
| 1 | NiCoFe-LDH | $Ru(bpy)_3$ $Cl_2$•$6H_2O$ | TEOA | MeCN-$H_2O$ (3 : 1 v/v) | 300 W Xe ($\lambda \geq 400$ nm) | $CH_4$: 56.6%<br>CO: 31.4%<br>$H_2$: 11.9% | **This work** |
| 2 | NiCoFe-LDH | $Ru(bpy)_3$ $Cl_2$•$6H_2O$ | TEOA | MeCN-$H_2O$ (3 : 1 v/v) | 300 W Xe ($\lambda \geq 500$ nm) | $CH_4$: 78.9%<br>CO: 19.3%<br>$H_2$: 1.71% | **This work** |
| 3 | Zr-bpdc/RuCO | $[Ru(phen)_3](PF_6)_2$ | TEOA | MeCN | 300 W Xe ($\lambda$ = 385-740 nm) | $CH_4$: 78.9%<br>CO: 19.3%<br>$H_2$: 1.71% | *Angew. Chem.*, **2016**, 55, 2697[1] |
| 4 | Iron tetra-phenylporphyrin complex | $Ir(ppy)_3$ | TEA | MeCN-$H_2O$ (2 : 1 v/v) | 300 W Xe ($\lambda > 420$ nm) | $CH_4$: 82%<br>$H_2$: 18% | *Nature*, **2017**, 548, 74[2] |
| 5 | Pt/C-$In_2O_3$ | Pt | TEOA | $H_2O$ | 300 W Xe | CO:63.3%<br>$CH_4$: 14.0%<br>$H_2$: 22.7% | *JACS*, **2017**, 139, 4123[3] |
| 6 | $In_2S_3$-$CdIn_2S_4$ | $Co(bpy)_3^{2+}$ | TEOA | MeCN-$H_2O$ (3:2 v/v) | 300 W Xe ($\lambda > 400$ nm) | CO: 70.2%<br>$H_2$:29.8% | *JACS*, **2017**, 139, 17305[4] |
| 7 | Ni(0.26%): CdS QD | -- | TEOA | $H_2O$ | 300 W Xe ($\lambda > 400$ nm) | CO: 11.2%<br>$CH_4$: 88.8% | *Angew.*, **2018**, 57, 16447[5] |
| 8 | Co1-G | $[Ru(bpy)_3]Cl_2$•$6H_2O$ | TEOA | MeCN | 300 W Xe ($\lambda > 420$ nm) | CO: 79.4%<br>$H_2$: 20.6% | *Adv. Mater.,* **2018**, 1704624[6] |
| 9 | Ni MOLs | $[Ru(bpy)_3]Cl_2$•$6H_2O$ | TEOA | MeCN | 300 W Xe ($\lambda > 420$ nm) | CO: 97.8 %<br>$H_2$: 2.2% | *Angew.,* **2018**, 57,16811[7] |
| 10 | $V_O$-rich $WO_3$ | -- | -- | $H_2O$ vapor | IR light | CO: below 3 | *Joule,* **2018**, 2, 1004[8] |
| 11 | Auc-C-M | -- | TEOA | MeCN | 300 W Xe ($\lambda > 420$ nm) | CO:72.7%<br>$CH_4$: 4.50%<br>$H_2$: 22.8% | *JACS,* **2018**, 140, 16514[9] |

| | | | | | | | |
|---|---|---|---|---|---|---|---|
| 12 | MAF-X27l-OH | $Ru(bpy)_3$ $Cl_2$•$6H_2O$ | TEOA | MeCN-$H_2O$ (4 : 1 v/v) | LED ($\lambda$ = 420 nm) | CO: 98.3%<br>$H_2$: 1.7% | *JACS*, **2018**, 140, 38[10] |
| 13 | NC@$NiCo_2O_4$ | $Ru(bpy)_3$ $Cl_2$•$6H_2O$ | TEOA | MeCN-$H_2O$ (3 : 2 v/v) | 300 W Xe ($\lambda$ > 420 nm) | CO: 88.5%<br>$H_2$: 11.5% | *Energy Environ. Sci.*, **2018**, 11, 306[11] |
| 14 | MOF-Ni | $Ru(bpy)_3$ $Cl_2$•$6H_2O$ | TIPA | MeCN-$H_2O$ (13 : 1 v/v) | 300 W Xe ($\lambda$ > 420 nm) | CO: 97.7%<br>$H_2$: 2.3% | *ACS Catal.,* **2019**, 9, 1726[12] |
| 15 | BIF-101 | $Ru(bpy)_3$ $Cl_2$•$6H_2O$ | TEOA | MeCN-$H_2O$ (4 : 1 v/v) | 300 W Xe ($\lambda$ > 420 nm) | CO: 72.3%<br>$H_2$: 17.7% | *JMCA*, **2019,**7,17272[13] |
| 16 | $Co_{1.11}Te_2CC$ | $Ru(bpy)_3$ $Cl_2$•$6H_2O$ | TEOA | MeCN-$H_2O$ (4 : 1 v/v) | 300 W Xe ($\lambda$ > 420 nm) | CO: 73.4%<br>$H_2$: 16.6% | *Chem. Commun.*, **2019**, 55, 6862[14] |
| 17 | NENU-606 | $Ru(bpy)_3$ $Cl_2$•$6H_2O$ | TEOA | $H_2O$ | 300 W Xe ($\lambda$ > 420 nm) | CO: 14.5%<br>$CH_4$: 85.5% | *Chem. Sci.*, **2019**, 10, 185[15] |
| 18 | $Co_3O_4$-NS | $Ru(bpy)_3$ $Cl_2$•$6H_2O$ | TEOA | $H_2O$ | LED lamp (400 nm-1000 nm) | CO:60.1%<br>$H_2$: 29.9% | *Appl. Catal. B-Environ.*, **2019**, 244, 996[16] |
| 19 | PMMCoCC-1200 | $Ru(bpy)_3$ $Cl_2$•$6H_2O$ | TEOA | MeCN-$H_2O$ (3 : 1 v/v) | 300 W Xe ($\lambda$ > 420 nm) | CO: 64.2%<br>$H_2$: 35.8% | *Small*, **2018**, 14, 1800762[17] |
| 20 | QA/rGO-2 | -- | TEOA | H2O | 300 W Xe ($\lambda$ > 420 nm) | CO:60.0%<br>$CH_4$: 36.7%<br>$H_2$: 3.3% | *Ind. Eng. Chem. Res.* **2019**, 58, 9636[18] |
| 21 | Monolayer NiAl-LDH | $Ru(bpy)_3$ $Cl_2$•$6H_2O$ | TEOA | MeCN-$H_2O$ (3 : 1 v/v) | 300 W Xe ($\lambda$ > 600 nm) | $CH_4$: 70.3%<br>CO: 29.7% | *Angew.*, **2019**, 58, 11860[19] |
| 22 | Pd/CoAl-LDH | $Ru(bpy)_3$ $Cl_2$•$6H_2O$ | TEOA | MeCN-$H_2O$ (3 : 1 v/v) | 300 W Xe ($\lambda$ > 600 nm) | CO : $H_2$ = 1.35 (Pd = 0)<br>CO : $H_2$ = 0.45 (Pd = 7.57%) | *J. Energy. Chem.,* **2019**, 2020, 46, 1-7[20] |

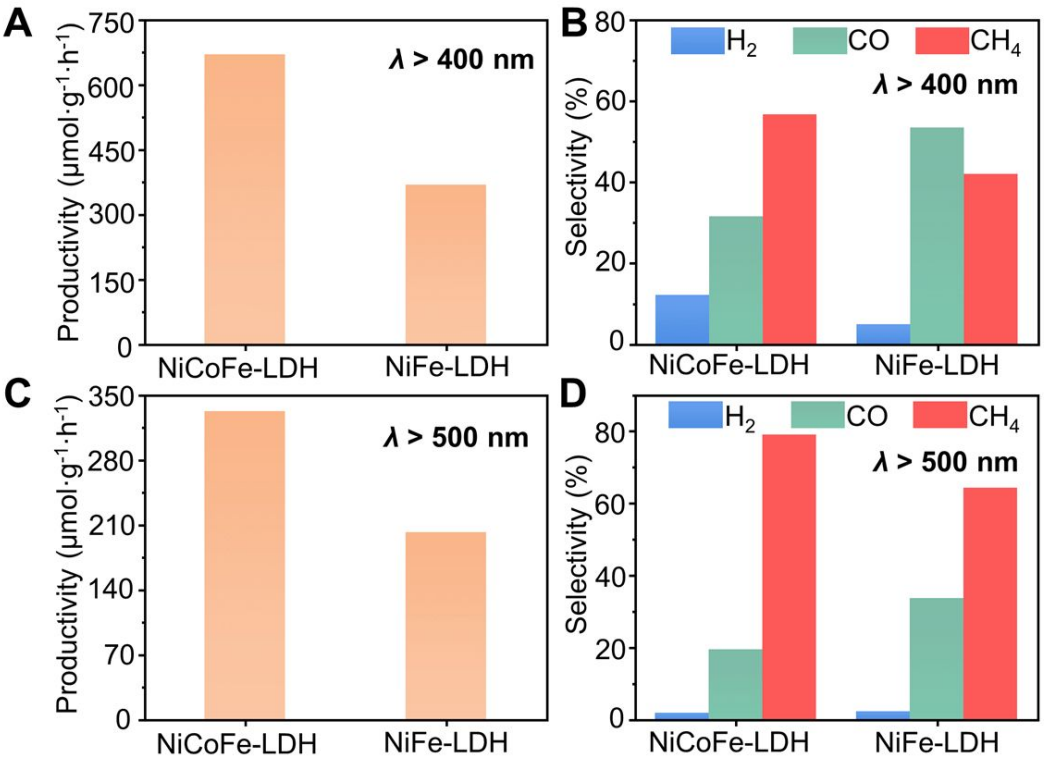


**Figure S12.** (A) $CO_2$ conversion rate (B) Selectivity of $CH_4$, CO, and $H_2$ under irradiation at $\lambda$ > 400 nm for NiCoFe-LDH and NiFe-LDH. (C) $CO_2$ conversion rate and (D) Selectivity of $CH_4$, CO, and $H_2$ on NiFe-LDH under irradiation $\lambda$ > 500 nm.

In order to further determine the role of Ni species, Co cations were completely replaced by Ni cations by increasing the amount of Ni species for the synthesis of NiFe-LDH. As shown in Figure S10A and B, compared with NiCoFe-LDH, the $CO_2$ conversion rate decreased from 670 μmol·g$^{-1}$·h$^{-1}$ (NiCoFe-LDH) to 368 μmol·g$^{-1}$·h$^{-1}$ (NiFe-LDH), while the selectivity of $CH_4$ had also been suppressed from 56.6% (NiCoFe-LDH) to 41.9% (NiFe-LDH).

More interesting, under light irradiation at $\lambda$ > 500 nm, the tendency kept a similar result, and the NiFe-LDH gave a lower $CO_2$ conversion rate and also the $CH_4$ selectivity also decreased to 64.3%. The above results indicated that further totally increasing Ni amount of NiCoFe-LDH for the synthesis of NiFe-LDH, both decreased $CO_2$ conversion and $CH_4$ selectivity further confirmed the advantage of trinary NiCoFe-LDH for the excellent photocatalytic $CO_2$ reduction to $CH_4$.

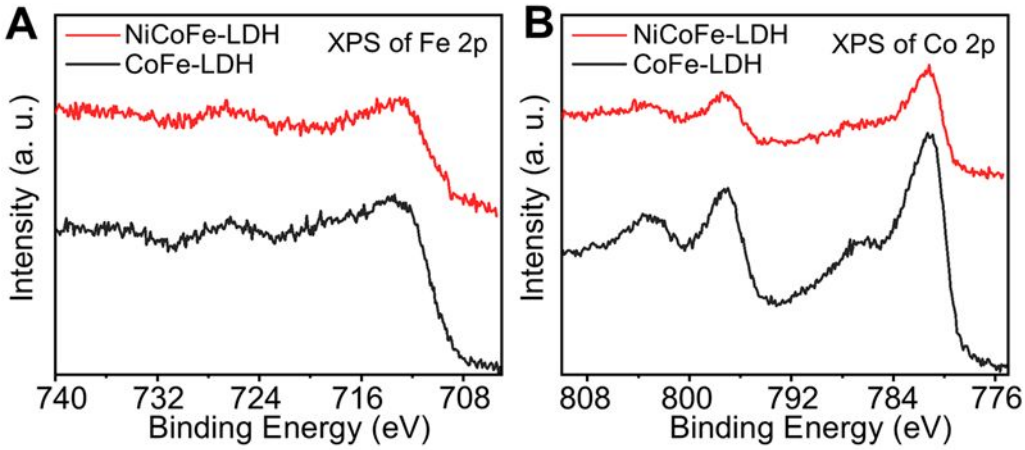


**Figure S13.** (A) Fe 2p X-ray photoelectron spectroscopy (XPS) and Co 2p XPS spectra of CoFe-LDH and NiCoFe-LDH, respectively.

**Table S3.** Local structure parameters around Co and Fe atoms estimated by EXAFS analysis

| Sample | Shell | $N^a$ | $R$[Å]$^b$ | $\sigma^2$ [$10^{-3}$ Å$^2$]$^c$ | $S_0^2$ | R-factor ($10^{-2}$) |
|---|---|---|---|---|---|---|
| **CoFe-LDH** | Fe-O | 6 | 2.00 | 4.4 | 0.82 | 0.79 |
| | Fe-M | 5.7 | 3.15 | 11.3 | | |
| | Co-O | 6 | 2.09 | 7.3 | 0.86 | 0.74 |
| | Co-M | 5.7 | 3.15 | 11.8 | | |
| **NiCoFe-LDH** | Fe-O | 5.2 | 1.98 | 5.4 | 0.82 | 0.87 |
| | Fe-M | 4.1 | 3.13 | 11.1 | | |
| | Co-O | 5.6 | 2.07 | 9.8 | 0.86 | 1.3 |
| | Co-M | 5.6 | 3.12 | 12.4 | | |

[a]$N$ = coordination number; [b]$R$ = distance between absorber and backscatter atoms; [c]$\sigma^2$ = Debye-Waller factor.

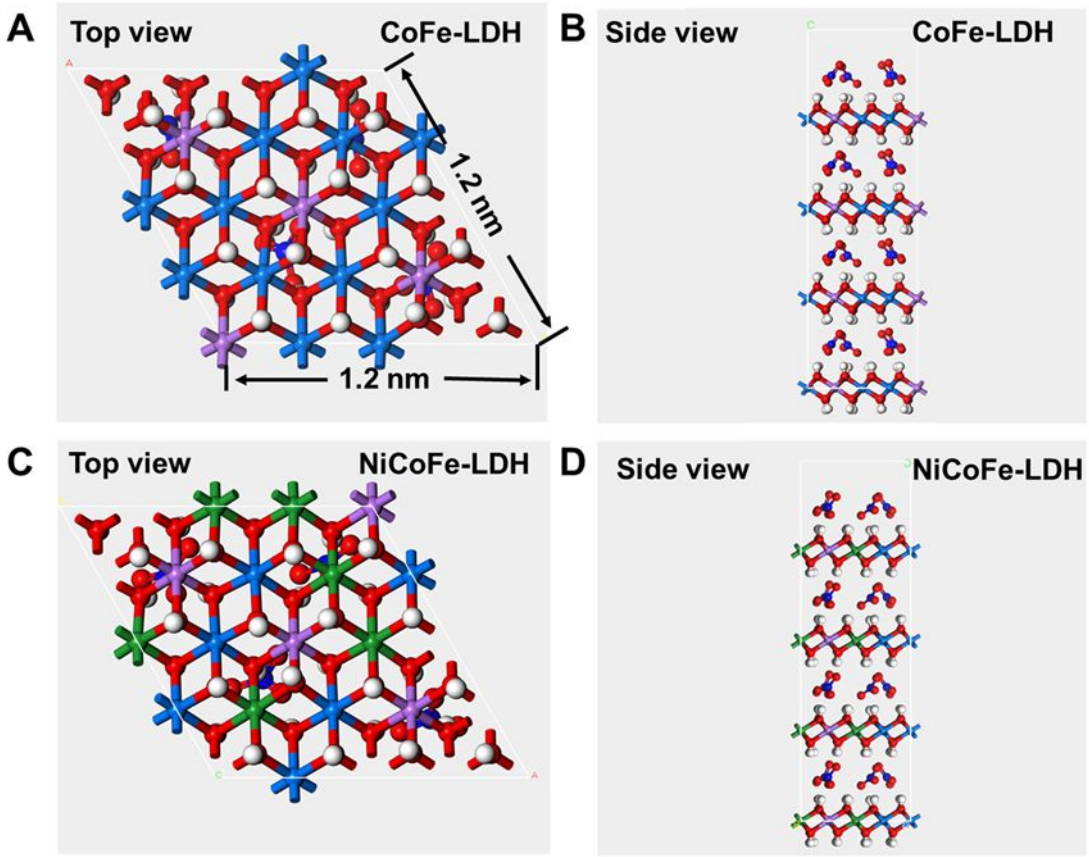


**Figure S14** Schematic illustration of layer structure of A, B) CoFe-LDH; C, D) NiCoFe-LDH, respectively.

The formula of NiCoFe-LDH is $Ni_{24}Co_{24}Fe_{16}H_{128}O_{128}$, and the surface area of this cell is 1.2 nm * 1.2 nm * sin 60° = 1.247 $nm^2$. The volume of the LDH can be obtained as follows: surface area of the cell * thickness (nm), where the thickness had been measured by AFM results. The corresponding oxygen number in this NiCoFe-monolayer model was 128, and total number of the metal (Ni, Co and Fe) was 64.

Ni species had occupied the position of Co after Ni was introduced into LDH structure, but there was no effect on the content of Fe species. Therefore, Fe element was used as the basis for calculating the corresponding vacancy density. As obtained from EXAFS results of NiCoFe-LDH, the corresponding coordination number of the first Fe-O shell was 5.2, compared with the ideal LDH with coordination number of 6.0, the ratio of defect concentration of Fe-O shell in NiCoFe-LDH was proposal to be around (5.2-6)/6 = 13.3%. Therefore, in the whole model, the defect intensity of oxygen vacancy can be inferred as followings:

Oxygen vacancies density ($nm^{-3}$) = ratio of the defect concentration * the total

oxygen number in the model per $nm^3$ = 13.3%*128/(1.247 $nm^2$ * 3.5 nm) = 3.90 $nm^{-3}$.

The above equation can be also extend to calculation the metal vacancies density, and the metal vacancies density ($nm^{-3}$) in NiCoFe-LDH = ratio of defect concentration * the total metal number in the model per $nm^3$ = (6.0-4.1)/6.0 * 64/(1.247 $nm^2$ * 3.5 nm) = 4.64 $nm^{-3}$

In summary, the defect density of $V_O$ or $V_M$ is showed in **Table S4:**

**Table S4.** the defect density of $V_O$ or $V_M$ in CoFe and NiCoFe-LDH calculated from the EAXFS data

| Sample | layer thickness | shell | $N^a$ | Defect density ($nm^{-3}$ ) |
|---|---|---|---|---|
| **CoFe-LDH** | 4.2 | Fe-O | 6 | -- |
| | 4.2 | Fe-M | 5.7 | 0.57 |
| **NiCoFe-LDH** | 3.5 | Fe-O | 5.2 | 3.90 |
| | 3.5 | Fe-M | 4.1 | 4.64 |

[a]$N$ = coordination number.

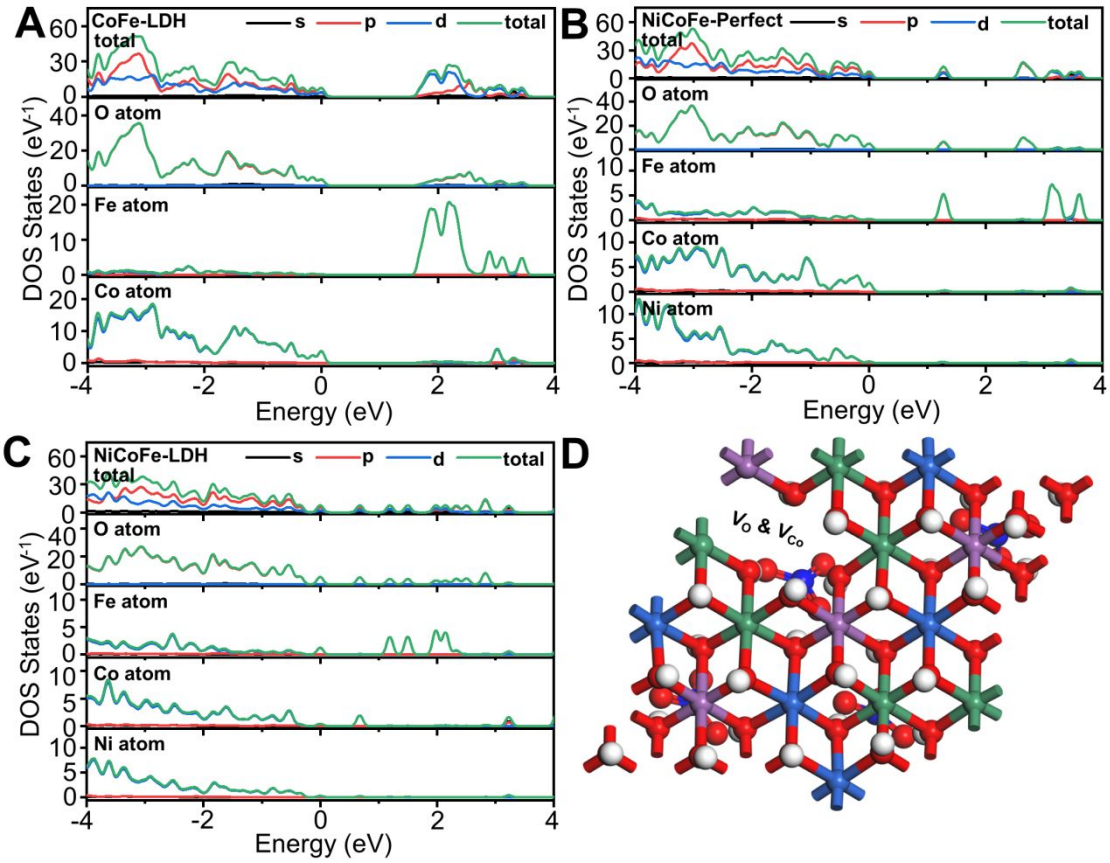


**Figure S15.** Total and partial electronic density of states (TDOS and PDOS) for (A) CoFe-LDH, (B) NiCoFe-Perfect, and (C) NiCoFe-LDH containing oxygen and metal vacancies. The Fermi energy level $E_F$ was set to zero. (D) Schematic structure model of NiCoFe-LDH containing vacancies.

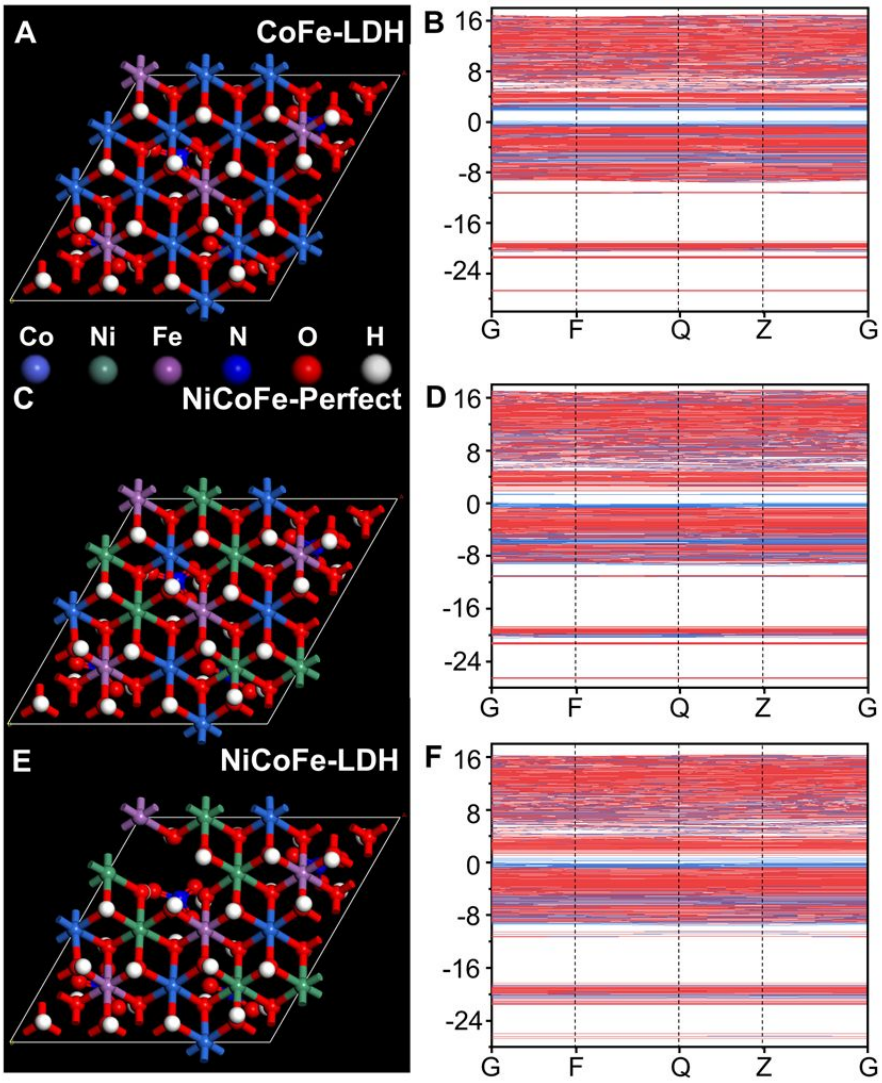


**Figure S16.** Schematic structure model and the corresponding calculated band structure for (A, B) CoFe-LDH, (C, D) NiCoFe-Perfect, and (E, F) NiCoFe-LDH containing oxygen and cobalt vacancies.

The direct energy gap was approximately 1.159 eV for NiCoFe-LDH, much lower than that of CoFe-LDH (1.707 eV).

## References


(1) Kajiwara, T.; Fujii, M.; Tsujimoto, M.; Kobayashi, K.; Higuchi, M.; Tanaka, K.; Kitagawa, S., Photochemical reduction of low concentrations of $CO_2$ in a porous coordination polymer with a ruthenium(II)-CO complex. *Angew. Chem. Int. Ed.* **2016,** *55*, 2697-2700.

(2) Rao, H.; Schmidt, L. C.; Bonin, J.; Robert, M., Visible-light-driven methane formation from $CO_2$ with a molecular iron catalyst. *Nature* **2017,** *548*, 74-77.

(3) Pan, Y. X.; You, Y.; Xin, S.; Li, Y.; Fu, G.; Cui, Z.; Men, Y. L.; Cao, F. F.; Yu, S. H.; Goodenough, J. B., Photocatalytic $CO_2$ reduction by carbon-coated indium-oxide nanobelts. *J. Am. Chem. Soc.* **2017,** *139*, 4123-4129.

(4) Wang, S.; Guan, B. Y.; Lu, Y.; Lou, X. W. D., Formation of hierarchical $In_2S_3$-$CdIn_2S_4$ heterostructured nanotubes for efficient and stable visible light $CO_2$ reduction. *J. Am. Chem. Soc.* **2017,** *139*, 17305-17308.

(5) Wang, J.; Xia, T.; Wang, L.; Zheng, X.; Qi, Z.; Gao, C.; Zhu, J.; Li, Z.; Xu, H.; Xiong, Y., Enabling visible-light-driven selective $CO_2$ reduction by doping quantum dots: trapping electrons and suppressing $H_2$ evolution. *Angew. Chem. Int. Ed.* **2018,** *57*, 16447-16451.

(6) Gao, C.; Chen, S.; Wang, Y.; Wang, J.; Zheng, X.; Zhu, J.; Song, L.; Zhang, W.; Xiong, Y., Heterogeneous single-atom catalyst for visible-light-driven high-turnover $CO_2$ reduction: the role of electron transfer. *Adv. Mater.* **2018,** *30*, 1704624.

(7) Han, B.; Ou, X.; Deng, Z.; Song, Y.; Tian, C.; Deng, H.; Xu, Y.-J.; Lin, Z., Nickel metal-organic framework monolayers for photoreduction of diluted $CO_2$: Metal-node-dependent activity and selectivity. *Angew. Chem. Int. Ed.* **2018,** *57*, 16811-16815.

(8) Liang, L.; Li, X.; Sun, Y.; Tan, Y.; Jiao, X.; Ju, H.; Qi, Z.; Zhu, J.; Xie, Y., Infrared light-driven $CO_2$ overall splitting at room temperature. *Joule* **2018,** *2*, 1004-1016.

(9) Cui, X.; Wang, J.; Liu, B.; Ling, S.; Long, R.; Xiong, Y., Turning Au nanoclusters catalytically active for visible-light-driven $CO_2$ reduction through bridging ligands. *J. Am. Chem. Soc.* **2018,** *140*, 16514-16520.

(10) Wang, Y.; Huang, N.-Y.; Shen, J.-Q.; Liao, P.-Q.; Chen, X.-M.; Zhang, J.-P., Hydroxide ligands cooperate with catalytic centers in metal-organic frameworks for efficient photocatalytic $CO_2$ reduction. *J. Am. Chem. Soc.* **2018,** *140*, 38-41.

(11) Wang, S.; Guan, B. Y.; Lou, X. W., Rationally designed hierarchical N-doped carbon@$NiCo_2O_4$ double-shelled nanoboxes for enhanced visible light $CO_2$ reduction. *Energy Environ. Sci.* **2018,** *11*, 306-310.

(12) Wang, X.-K.; Liu, J.; Zhang, L.; Dong, L.-Z.; Li, S.-L.; Kan, Y.-H.; Li, D.-S.; Lan, Y.-Q., Monometallic catalytic models hosted in stable metal-organic frameworks for tunable $CO_2$ photoreduction. *ACS Catal.* **2019,** *9*, 1726-1732.

(13) Hong, Q.-L.; Zhang, H.-X.; Zhang, J., Synthesis of boron imidazolate frameworks with cobalt clusters for efficient visible-light driven $CO_2$ reduction. *J. Mater. Chem. A* **2019,** *7*, 17272-17276.

(14) Xu, Y.; Mo, J.; Xie, G.; Ding, D.; Ding, S.; Wang, X.; Li, C., MOF-derived $Co_{1.11}Te_2$ with half-metallic character for efficient photochemical conversion of $CO_2$ under visible-light irradiation. *Chem. Commun.* **2019,** *55*, 6862-6865.

(15) Xie, S.-L.; Liu, J.; Dong, L.-Z.; Li, S.-L.; Lan, Y.-Q.; Su, Z.-M., Hetero-metallic active sites coupled with strongly reductive polyoxometalate for selective photocatalytic $CO_2$-to-$CH_4$ conversion in water. *Chem. Sci.* **2019,** *10*, 185-190.

(16) Chen, W.; Han, B.; Tian, C.; Liu, X.; Liang, S.; Deng, H.; Lin, Z., MOFs-derived ultrathin holey $Co_3O_4$ nanosheets for enhanced visible light $CO_2$ reduction. *Appl. Catal. B-Environ.* **2019,** *244*, 996-1003.

(17) Zhao, K.; Zhao, S.; Gao, C.; Qi, J.; Yin, H.; Wei, D.; Mideksa, M. F.; Wang, X.; Gao, Y.; Tang, Z.; Yu, R., Metallic cobalt-carbon composite as recyclable and robust magnetic photocatalyst for efficient $CO_2$ reduction. *Small* **2018,** *14*, 1800762.

(18) Yang, P.; Guo, S.; Yu, X.; Zhang, F.; Yu, B.; Zhang, H.; Zhao, Y.; Liu, Z., Photocatalytic reduction of carbon dioxide over quinacridone nanoparticles supported on reduced graphene oxide. *Ind. Eng. Chem. Res.* **2019,** *58*, 9636-9643.

(19) Tan, L.; Xu, S.-M.; Wang, Z.; Xu, Y.; Wang, X.; Hao, X.; Bai, S.; Ning, C.; Wang, Y.; Zhang, W.; Jo, Y. K.; Hwang, S. J.; Cao, X.; Zheng, X.; Yan, H.; Zhao, Y.; Duan, H.; Song, Y.-F., Highly selective photoreduction of $CO_2$ with suppressing $H_2$ evolution over monolayer layered double hydroxide under irradiation above 600 nm. *Angew. Chem. Int. Ed.* **2019,** *58*, 11860-11867.

(20) Wang, X.; Wang, Z.; Bai, Y.; Tan, L.; Xu, Y.; Hao, X.; Wang, J.; Mahadi, A. H.; Zhao, Y.; Zheng, L.; Song, Y.-F., Tuning the selectivity of photoreduction of $CO_2$ to syngas over Pd/layered double hydroxide nanosheets under visible-light up to 600 nm. *J. Energy. Chem.* **2020**, *46*, 1-7.